

## Article

# An Integration of Logistic Regression and Geographic Information System for Development of a Landslide Hazard Index to Land Use: A Case Study in Pingtung County in Southern Taiwan

Chih-Ming Tseng <sup>1,\*</sup>, Yie-Ruey Chen <sup>2</sup>, Ching-Ya Tsai <sup>3</sup> and Shun-Chieh Hsieh <sup>2</sup><sup>1</sup> Department of Hydraulic and Ocean Engineering, National Cheng Kung University, Tainan 701401, Taiwan<sup>2</sup> Department of Land Management and Development, Chang Jung Christian University, Tainan 711301, Taiwan; yrchen@mail.cjcu.edu.tw (Y.-R.C.); sch@mail.cjcu.edu.tw (S.-C.H.)<sup>3</sup> Disaster Prevention Research Center, National Cheng Kung University, Tainan 701401, Taiwan; h64371281@gmail.com

\* Correspondence: cmtseng@gs.ncku.edu.tw

**Abstract:** In Taiwan, mountainous areas account for approximately two-thirds of the total area. The steep terrain and concentrated rainfall during typhoons cause landslides, which pose a considerable threat to mountain settlements. Therefore, models for analyzing rainfall-induced landslide hazards are urgently required to ensure adequate land use in mountainous areas. In this study, focusing on Pingtung County in southern Taiwan, we developed a landslide hazard index ( $I_{RL}$ ) to land use. Using FORMOSA-2 and SPOT-5 satellite images, data were collected before and after four typhoons (one in 2009 and three in 2013). The ArcGIS random tree classifier was used for interpreting satellite images to explore surface changes and disasters, which were used to analyze slope disturbances. The product of the maximum 3-h rolling rainfall intensity and effective accumulated rainfall was used as a rainfall trigger index ( $I_{RT}$ ). Considering environmental and slope disturbance factors, an index of slope environmental strength potential ( $I_{SESP}$ ) was developed through logistic regression (LR). Landslide hazard to land use was estimated using  $I_{RT}$  and  $I_{SESP}$ . The average coefficient of agreement (Kappa) was approximately 0.71 (medium to high accuracy); the overall accuracy of slope environmental strength potential analysis was approximately 80.4%. At a constant  $I_{SESP}$ ,  $I_{RT}$  increased with the increasing hazard potential of rainfall-induced landslides. Furthermore,  $I_{RT}$  and  $I_{SESP}$  were positively correlated with landslide occurrence. When large  $I_{SESP}$  values occur (e.g., fragile environment and high land development intensity), small  $I_{RT}$  values may induce landslides.

**Keywords:** land use; mountainous area; rainfall; landslide hazard; random tree classifier; logistic regression; geographic information system; Taiwan



**Citation:** Tseng, C.-M.; Chen, Y.-R.; Tsai, C.-Y.; Hsieh, S.-C. An Integration of Logistic Regression and Geographic Information System for Development of a Landslide Hazard Index to Land Use: A Case Study in Pingtung County in Southern Taiwan. *Water* **2024**, *16*, 1038. <https://doi.org/10.3390/w16071038>

Academic Editors: Qingzhao Zhang and Danyi Shen

Received: 18 February 2024

Revised: 29 March 2024

Accepted: 3 April 2024

Published: 4 April 2024



**Copyright:** © 2024 by the authors. Licensee MDPI, Basel, Switzerland. This article is an open access article distributed under the terms and conditions of the Creative Commons Attribution (CC BY) license (<https://creativecommons.org/licenses/by/4.0/>).

## 1. Introduction

Taiwan is an island located in the North Pacific subtropical monsoon region, which is vulnerable to typhoons. More than two-thirds of Taiwan's total area is mountainous with steep slopes. Recently, climate anomalies have resulted in frequent extreme rainfall events. The number of typhoons that hit Taiwan has increased every year, and large-scale landslides and debris flows have become likely. As stated in the 2012 White Paper on Disaster Management [1], remote mountainous settlements in Chiayi County, Kaohsiung City, Tainan City, Pingtung County in southern Taiwan account for approximately 24% of the total area in Taiwan. Recent large-scale sediment disasters due to typhoon-induced concentrated rainfall occurred mostly in the remote mountainous areas of southern Taiwan. Such disasters pose a major threat to the environmental security of the settlements in remote mountainous areas. For example, Typhoon Morakot on August of 2009, with a maximum precipitation of over 2884 mm in 5 days, induced over 22,705 landslides, covering

a total area of 274 km<sup>2</sup> in mountainous area throughout southern Taiwan [2]. Typhoon Morakot resulted in 619 deaths, 76 missing persons, and the temporary evacuation of 24,950 residents, flooding, and approximate USD five billion in economic losses [3]. Since Typhoon Morakot struck, the slopes of the remote mountainous areas of southern Taiwan have become highly unstable. Therefore, studies on the land use risk of the aforementioned settlements during rainfall disasters are essential.

Jan and Lee [4] used the product of effective accumulated rainfall (*EAR*) and rainfall intensity as a rainfall trigger index ( $I_{RT}$ ) for determining debris flow; they discovered relevant geological factors (average stream bed slope, catchment area, landslide rate, and lithology) for establishing comprehensive geological indicators. A rainfall prediction model for debris flow was constructed using the rainfall warning and comprehensive physiographic indices. For rainfall warning, the following occurrence possibilities were set: 10%, 50%, and 90%. Chen et al. [5] demonstrated that extreme rainfall events cause frequent landslide erosion; they reported that a maximum 24-h rainfall amount of >600 mm resulted in the average landslide erosion rate of 64–79%. Jan et al. [6] mentioned that the effects of typhoon rainfall depend not only on the rainfall amount but also on its intensity. Tseng et al. [7] reported that the number and area of rainfall-induced landslides were positively correlated with the degree of land disturbance. Chen et al. [8] investigated areas with high and low susceptibility to landslides; they identified cumulative rainfall to be the primary factor for landslide occurrence in areas with high susceptibility; in contrast, in areas with low susceptibility, the rainfall intensity was found to be the key factor. Due to climate extremes, areas with high susceptibility exhibited a higher magnitude and frequency of landslides than those with low susceptibility.

Lee et al. [9] explored the mechanisms underlying landslide disasters due to the intensity of Typhoon Soudelor-induced rainfall on the mountainous areas of northern Taiwan; they revealed that most sediment disasters occurred 1 or 2 h after peak rainfall. Moreover, the maximum rainfall occurring 3, 6, and 12 h after this event was higher than that in the 200-year return period. To estimate a rainfall alert value for landslide occurrence, Caracciolo et al. [10] analyzed historical data on the rainfall that led to a landslide as well as data on rainfall occurring 5, 15, and 30 days before a landslide in southern Sicily, Italy. Chen and Wu [11] focused on a state-owned forest land in Taiwan and analyzed various internal (e.g., elevation, slope, terrain roughness, distance from the fault, and distance from the river) and external (total accumulated rainfall after event) factors through logistic regression (LR) to build an internal potential level without external factors; subsequently, they evaluated the changes in the potential value and rainfall to estimate a reference value for the prediction of landslides induced by rainfall. Shahabi et al. [12] combined remote sensing and a geographic information system (GIS) to statistically delineate areas susceptible to landslides; for this, they considered the following factors: slope, aspect, elevation, lithology, normalized difference vegetation index, vegetation, rainfall, distance from the fault, distance from the river, and distance from the road. Tseng et al. [7] focused on the periods before and after a typhoon that recently caused a road slope landslide in the study area; through image interpretation, they identified surface changes before and after the landslide disaster and developed a model for assessing landslide susceptibility. Then, the GIS platform was used to construct landslide susceptibility maps. Among the statistical methods used for evaluating landslide susceptibility, LR analysis has been proven to be one of the most reliable approaches [13–20].

In the past, studies seldom focused on the landslide hazard to land use, therefore models for analyzing rainfall-induced landslide hazards to ensure adequate land use in mountainous areas are necessary. The data processing and flowchart of research work of the present study is shown in Figure 1. Coupled with the use of the ArcGIS platform, random tree classifier (RTC) was employed to classify and interpret satellite images to obtain land use information and disasters. Furthermore, considering the regional environmental characteristics and land disturbance, we analyzed the potential of slope environmental intensity, factors associated with slope disasters, and the rainfall characteristics of the study

area and investigated the correlation between rainfall trigger and slope environmental strength potential to develop  $I_{RL}$ . Our research findings can provide considerable references for the strategies of land use in mountainous settlements. However, only the influence from the natural environment was considered; the socio-economic, governmental policy aspects that should be overall considered in decision making for land use were excluded in this study. This could lead to the potential research direction in the next step.

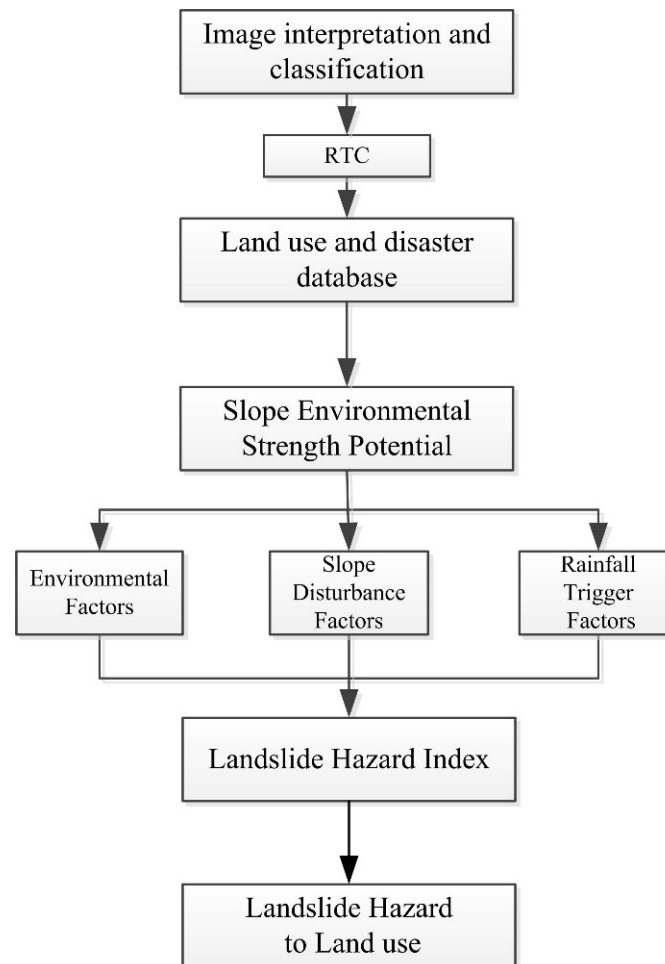


**Figure 1.** Flowchart of the research work.

## 2. Methods and Materials

### 2.1. Study Area

This study was conducted in Sandimen Township and certain mountainous areas of Wutai Township in Pingtung County in southern Taiwan (Figure 2). Pingtung County is located in the south of the Tropic of Cancer. Except for elevated mountainous areas, the county has a tropical monsoon climate and the temperature does not vary substantially throughout the year. The annual average temperature and rainfall is approximately 25.5 °C and 2325 mm, respectively. It is humid and rainy in summer. However, because of the barrier between the Dawu Mountain Range and the Central Mountain Range, the cold northeast monsoon is blocked from entering the county; this blockage, combined with a low latitude and sufficient sunshine, reduces the intensity of winter in Pingtung, where the average high and low temperatures are 24–27 °C and 16–19 °C, respectively [21,22]. In Sandimen and Wutai Townships, most of the strata are Chaozhou and Bilushan Formations; low contents of alluvial and grounding deposits are observed. Lithologically, the study area is mainly interbedded with hard shale, slate, and sandy shale. In addition, low contents of gravel, sand, clay, and slate interbedded with metamorphic sandstone and metamorphic igneous rock lens, mud, sand, and gravel, lenticular sandstone bodies are noted [23].

Sandimen Township is located at an altitude of 100–2159 m and at the intersection of mountains and plains and features, mostly hilly terrain. Wutai Township is located in the northeast area of Pingtung County (in the Central Mountain Range). This township has steep terrain and is located at an average altitude of >1000 m. The largest tributary flowing through the study area is the Ailiao River, which is the largest tributary of the Gaoping River. Its farthest source stream is Eluowu River, which flows south to Babanaban River and then turns southwest to Laibuan River (where it is called the Ailiao North Stream); subsequently, it turns south to join Hayou Creek and Qiaoguo Laci Creek (among others) and finally turns south to converge into Ailiao South Stream in Dalai Village; this is called Ailiao Creek in Sandimen Township. The main rivers in Wutai Township are Erchong and Ailiao Beixi, whereas the main rivers in Wutai Township are Ailiao Beixi and Qiaogulaci [21].



**Figure 2.** Study area.

In Sandimen Township, the Sandi and Dalai villages have the highest ( $n = 1683$ ) and lowest ( $n = 402$ ) populations, respectively. In Wutai Township, Wutai and Jilou Villages have the highest ( $n = 1325$ ) and lowest ( $n = 210$ ) populations, respectively [24]. The residents of Sandimen Township are mainly Paiwan individuals (Taiwan Aborigines); some Rukai individuals also reside in this township such as in Qingye Village, which has recently been included in the Maolin National Scenic Area. The main economy in Sandimen Township is agriculture, and the main agricultural products are sweet potato, millet, taro, mango, pineapple, red quinoa, and coffee [25]. The residents of Wutai Township are mainly Rukai individuals [26]. The main agricultural products of the township are love jade, red quinoa, millet, coffee, taro, and sweet potato [27].

## 2.2. Image Interpretation and Classification

### 2.2.1. Preprocessing of Satellite Images

FORMOSA 2 (FS-2) or SPOT-5 satellite images of the areas affected by typhoons or rainstorms were acquired. Data on the 2009 Typhoon Morakot, 0517 rainfall in 2013, 2013 Typhoon Soulik, and 2013 Typhoon Kongrey were obtained to explore the land development types and landslide areas in the study area. We used six satellite images with image resolutions of  $8\text{ m} \times 8\text{ m}$  and  $10\text{ m} \times 10\text{ m}$  (Table 1).

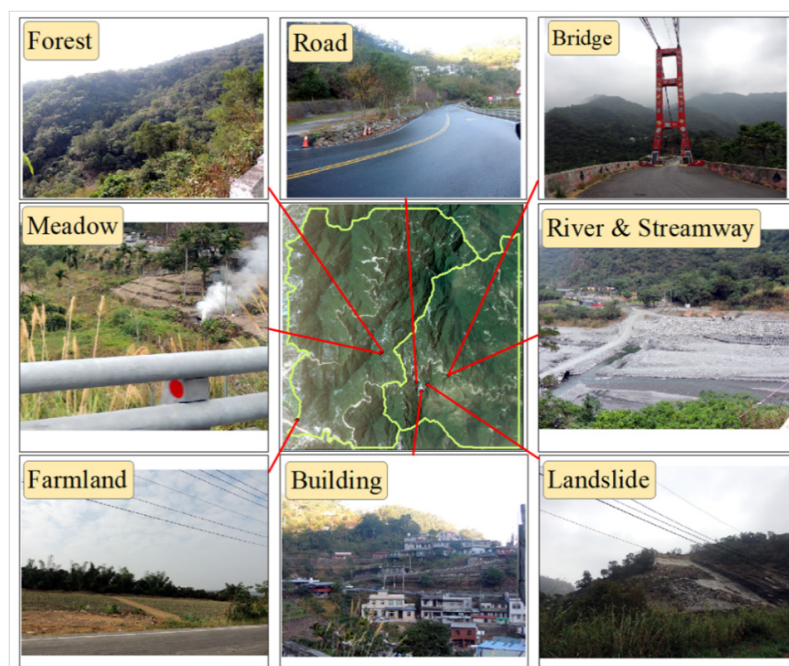
**Table 1.** Basic satellite imagery data.

Image Shooting Date	Before/after Event	Image Resolution	Type	Location	X TWD97	Y TWD97
22 July 2009	Before Typhoon Morakot	8 m × 8 m		Upper left	211584	2530416
9 May 2009						
15 August 2009						
11 January 2010	After Typhoon Morakot	8 m × 8 m		Bottom right	230432	2511176
15 January 2013						
19 January 2013	Before 0517 Rainfall	8 m × 8 m	FS-2			
3 June 2013						
29 June 2013	After 0517 Rainfall	8 m × 8 m		Upper left	211584	2530408
27 August 2013						
11 September 2013	Before Typhoon Soulik	8 m × 8 m		Bottom right	230424	2511184
27 August 2013						
11 September 2013	After Typhoon Soulik	8 m × 8 m				
11 September 2013						
9 September 2013	After Typhoon Kongrey	10 m × 10 m	SPOT-5	Upper left	211570	2530430
9 September 2013						
				Bottom right	230440	2511160

The FS-2 and SPOT-5 satellite images are multispectral and contain four spectral bands [28]. FS-2 spectral bands are red, green, blue, and near-infrared (NIR), whereas SPOT-5 spectral bands are red, green, NIR, and short-wave infrared. The telemetry image processing software ERDAS IMAGINE (2013) [29] was used to fuse and locate the images.

### 2.2.2. Selection of Satellite Imagery Classifications

In this study, FS-2 or SPOT-5 satellite images of four typhoons or rainstorms were selected as the base map. Using GIS ArcGIS, each classification factor was manually digitized and circled. We compared the Tiff files of the satellite images (resolution, 2 m × 2 m) of the study area to increase the accuracy of the sampling area delineation; furthermore, we selected the following eight classifications suitable for the scope of this study: river, road, building, farmland, forest, meadow, streamway, and bare land (Figure 3).



**Figure 3.** Current land use in the study area.

### 2.3. Rainfall Projection

#### 2.3.1. Effective Accumulative Rainfall (EAR)

We referred to the rainfall analysis methods described by Seo and Funasaki [30] and Tseng et al. [7]. Concentrated rainfall is considered to be continuous if no rainfall occurs 24 h before and after the rainfall event. The rainfall field with continuous rainfall inducing a landslide is regarded as the main rainfall field. The beginning of rainfall was defined as the time point when the first rainfall reached  $\geq 4$  mm in the main rainfall field. Cumulative rainfall inducing a landslide was calculated. Cumulative rainfall was divided into previous indirect rainfall ( $P_b$ ) and previous direct rainfall ( $P_r$ ). Previous indirect rainfall refers to the amount of rainfall in the main rainfall field within 7 days [30] and can be calculated using Equation (1).

$$\sum_{n=1}^7 k^n P_n = P_b \quad (1)$$

where  $P_n$  is the amount of rainfall (mm) in  $n$  days before the main rainfall field;  $k$  is the decreasing coefficient. In the present study,  $k$  was 0.9 [31]. EAR can be calculated as follows:

$$EAR = P_r + P_b \quad (2)$$

where  $P_r$  is the amount of cumulative rainfall from the first rainfall in the main rainfall field from the time of the landslide disaster (a time point when the first rainfall reaches  $\geq 4$  mm) to the occurrence of the landslide.

#### 2.3.2. Rolling Rainfall Intensity

Rain-induced landslides may be triggered by continuous rainfall for several hours. Therefore, rolling rainfall intensity can be expressed using Equation (3):

$$I_{mR} = \sum_{i=t-m+1}^m I_i = I_{t-m+1} + I_{t-m+2} + \dots + I_m \quad (3)$$

where  $I$  is the rainfall intensity,  $m$  is the unit time of rain rolling, and  $m = 3$  h [7].  $I_{mR}$  is the  $I_R$  in  $m$  h, and  $I_t$  is the rainfall intensity in  $t$  h.

### 2.4. Random Tree Classifier (RTC)

We used the RTC in the ArcGIS supervised image classification module to classify images. The RTC does not lead to overfitting and can process segmented images and auxiliary grid datasets [32]. The classifier can be used to construct several decision trees, and selects a random subset of variables for each tree and uses the most frequent tree output for the overall classification. Therefore, random trees correct for the tendency of decision trees to overfit the training data. Random trees are a collection of individual decision trees; each tree is generated from different subsets of sample and training data. Decisions are made in the order of the importance of each pixel being classified. An image is drawn for a certain pixel that appears as a tree branch. After the entire dataset is processed, each branch forms a whole tree; this is the concept of random trees. In the operation of random trees, each tree has decision-making power; this process reduces overfitting. In the random tree method, analogically, many trees continue to grow; the changes in the trees of a forest are projected into randomly selected subspaces through training data, and each node's decision is optimized through a random process [32].

### 2.5. Logistic Regression (LR)

In regression analysis, dependent variables serve as categorical variables, whereas independent variables serve as continuous or dummy variables. Dummy variables represent categorical data; the corresponding numerical values are the basis for classification and have no comparative significance. The primary feature of LR is that dependent variables are categorical variables, whereas independent variables can be continuous or categorical variables [33].

LR is used for analyzing dichotomous dependent variables. One or more independent variables may be included in the model. Response variables can be categorical or continuous variables. Previously, landslide susceptibility was analyzed by mostly considering the distribution patterns of binary variables [34]. Through a statistical induction method, a set of regression patterns may be identified to differentiate between landslide and non-landslide. The value range of the logistic distribution function is 0–1, and the distribution of the value range follows an S-shaped curve [35].

As shown in Equation (4), linear regression assumes a linear function and includes dependent and independent variables (and random residual values) [33].

$$Y = \beta_0 + \beta_1 \times x_1 + \beta_2 \times x_2 + \beta_3 \times x_3 + e \quad (4)$$

where  $Y$  is a dependent variable;  $x_1$ ,  $x_2$ , and  $x_3$  are independent variables; and  $e$  represents a residual value.  $\beta_0 + \beta_1x_1 + \beta_2x_2 + \beta_3x_3$  is a linear function between expectation  $E(Y)$  and the three independent variables.

LR is used to construct practical and reasonable allocation models for predicting the correlations between a dependent variable ( $y$ ) and a set of independent variables ( $x$ ). The relationship usually refers to the relationship between a set of independent variables ( $x_s$ ), which is used to predict the probability of the dependent variable being equal to 1 such as the probability of landslide occurrence. The ratio of the probability of event occurrence to that of event non-occurrence is called the event odds. A linear function can be obtained using its natural logarithm, which is the logit model, as shown in Equation (5) [33].

$$\ln\left(\frac{P}{1-P}\right) = \alpha + \sum_{i=1}^k \beta_i x_i \quad (5)$$

where  $P$  is an independent variable;  $x_1, x_2, \dots, x_k$  are the probabilities of event occurrence. In this study,  $y$  indicates the probability of landslides, and the aforementioned  $x$  parameters represent various independent variables. A logistic curve can be constructed using the logit function; its mathematical formula is shown in Equation (6).

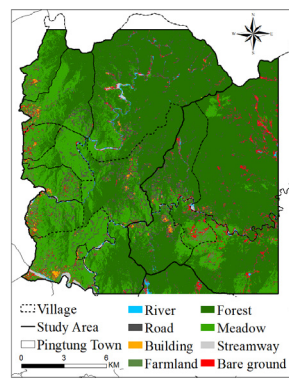
$$P = \frac{1}{1 + e^{-(\alpha + \sum_{i=1}^k \beta_i x_i)}} \quad (6)$$

In general, the probability threshold is set at 0.5. A predicted probability ( $p$ ) of  $\geq 0.5$  indicates the likelihood of a landslide event; in contrast, if  $p < 0.5$ , a landslide event is not expected to occur.

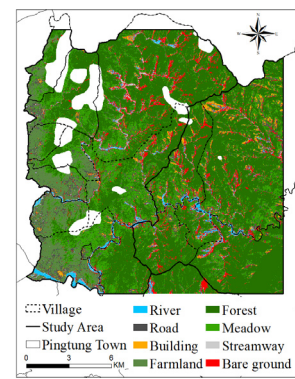
### 3. Results

#### 3.1. Interpretation of Images and Assessment of Accuracy

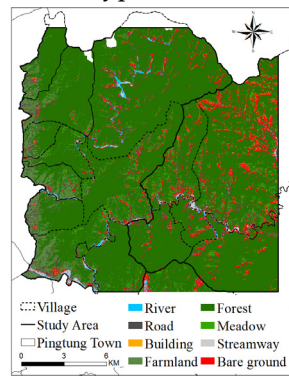
Considering the aforementioned eight classifications, the RTC module was used with the results of texture analysis to interpret the images. The research scope was interpreted using a total of six satellite images obtained before and after the 2009 Typhoon Morakot, 0517 rainfall in 2013, 2013 Typhoon Soulik, and 2013 Typhoon Kongrey. Figure 4 depicts the results of image interpretation. To confirm the accuracy of the interpretation results, we randomly selected a total of 25 points (interpretation grids; checkpoints) for each classification and compared them with high-resolution aerial photos and on-site survey data. The most common accuracy evaluation method is the error matrix [36], which is used to calculate the coefficient of agreement (Kappa index) and overall accuracy. The value of the Kappa index proposed by Cohen [37] ranges from 0 to 1. Kappa values of  $< 0.4$ ,  $0.4\text{--}0.8$ , and  $> 0.8$  indicate low, medium, and high accuracies, respectively. Table 2 summarizes the OAs before and after the rainfall events in the study area. In this study, the average Kappa value of each satellite image was approximately 0.71, and the average overall accuracy was approximately 74% (medium to high accuracy).



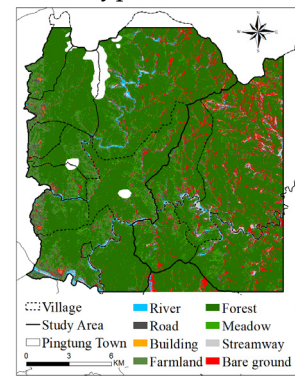
Before Typhoon Morakot



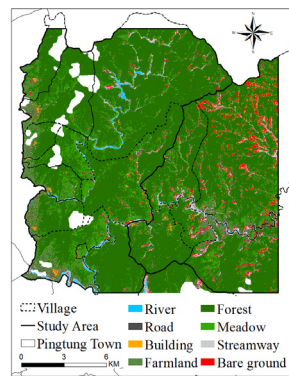
After Typhoon Morakot



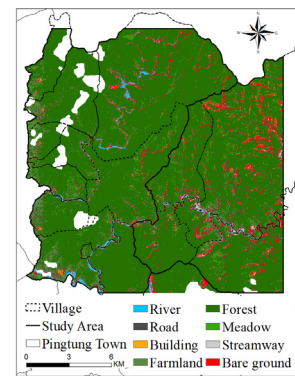
Before 0517 rainfall



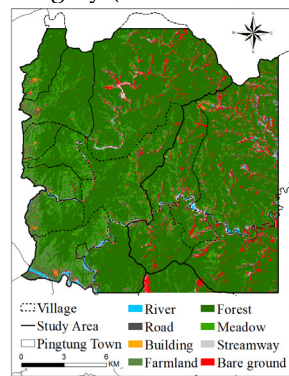
After 0517 rainfall and before Typhoon Soulik



After Typhoon Soulik and before Typhoon Kongrey (resolution, 8 m)



After Typhoon Soulik and before Typhoon Kongrey (resolution, 10 m)



After Typhoon Kongrey

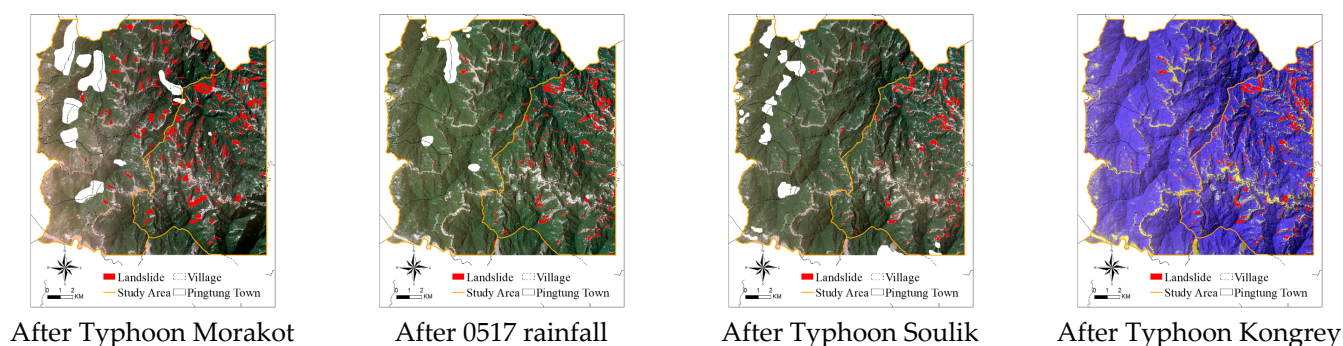
Figure 4. Images obtained before and after various rainfall events.

**Table 2.** Coefficients of agreement and overall accuracies of the satellite image interpretation results.

Year	Rainfall Event	Resolution	Kappa	OA (%)
2009	Before Typhoon Morakot	8 m	0.66	70.0
	After Typhoon Morakot	8 m	0.70	73.0
2013	Before 0517 rainfall	8 m	0.69	72.5
	After 0517 rainfall and before Typhoon Soulik	8 m	0.70	73.3
	After Typhoon Soulik and Before Typhoon Kongrey	8 m	0.78	79.5
	After Typhoon Soulik and Before Typhoon Kongrey	10 m	0.77	79.5
	After Typhoon Kongrey	10 m	0.74	76.5

### 3.2. Identification of Landslides through Image Interpretation

After image classification, to identify rainfall-induced landslides in the study area, we subtracted bare land grids before and after rainfall events by using the image subtraction method. The river, streamway, and bare land classifications with a slope percentage of <5% were deducted. High-resolution aerial photos of the study area were compared, and manual inspection was performed to identify landslides; then, the locations of the rainfall-induced landslides in the study area were obtained (Figure 5). Among the types of slope failure, debris slides were the easiest and most reliable type to be identified in the satellite images since vegetation was effectively stripped off from the slopes. Therefore, debris slides are the major landslides mapped in our study. The 2009 Typhoon Morakot resulted in the highest rainfall and the largest landslide area (1313.12 ha). The areas of landslides induced by the other events were as follows: 0517 rainfall in 2013, 813.92 ha; Typhoon Kongrey, 789.44 ha; and Typhoon Soulik, 635.04 ha.

**Figure 5.** Distribution map of landslides occurring after various rainfall events.

### 3.3. Development of a Model for Assessing Rainfall-Induced Landslide Susceptibility

#### 3.3.1. Selection of Factors Associated with Landslide

Landslides can be attributed to factors such as artificial slope land use, environment, and rainfall triggers. Human activities may negatively affect water and soil conservation on slope lands, which compromises the safety of slope land. Therefore, referring to studies of Chen et al. [38] and Tseng et al. [7], we divided the aforementioned factors into the following three categories: environmental, slope disturbance, and rainfall trigger factors. The environmental factors assessed in this study included elevation, slope, aspect, slope roughness, terrain roughness, distance from the river, and geology. The slope disturbance factors included road density, building density, farmland planting rate, forest density, grassland density, and bare density. The rainfall trigger factor was the product of EAR and the maximum 3-h rolling rainfall intensity ( $I_{3R,max}$ ).

The digital elevation model (DEM) was used to analyze the environmental factors using ArcGIS Spatial Analyst. A basic grid of 40 m × 40 m was constructed for the factors

related to landslide occurrence, followed by the development of a GIS database of the study area. The hazard factors are described below.

#### Environmental Factors

- Elevation (*El*)

The elevation of a place refers to its height from the sea level. In Taiwan, the elevation datum comprises the mean sea level of Keelung Port, and the elevation of the terrain is called the elevation difference. When other factors are constant, higher degrees of elevation are associated with a higher sliding force. We used a 20 m × 20 m DEM for analysis. The elevation of the study area is 78–2437 m, which was divided into a total of seven grades and coded. Table 3 presents the elevation classification codes, ranging from an elevation of <350 m coded as 1 to an elevation of >2100 m coded as 7.

**Table 3.** Elevation codes.

Grade Range of Elevation (m)	Code
Above 2101	7
1751–2100	6
1401–1750	5
1051–1400	4
701–1050	3
351–700	2
Below 350	1

- Slope (*Sl*)

Here, slope indicates the inclination of a slope. Higher degrees of inclination indicate steeper slopes and vice versa. High inclination as well as poor soil and water conservation may facilitate the development of landslides. In this study, the slope value of each grid was obtained through DEM and ArcGIS slope analysis. According to the Classification Standards for Land Utilization Limits of Hillside Lands outlined in the Regulations of Soil and Water Conservation [39], we graded and coded slopes (Table 4). A first-grade slope was coded as 1, whereas a seventh-grade slope was coded as 7.

**Table 4.** Slope codes.

Slope Grade	Grade Range of Slope (%)	Code
7	Above 100	7
6	50–100	6
5	40–55	5
4	30–40	4
3	15–30	3
2	5–15	2
1	Below 5	1

- Slope Roughness (*Slr*)

Slope roughness reflects the changes in a slope (standard deviation). Higher degrees of slope roughness indicate higher extents of changes, which may facilitate the occurrence of landslides. Cluster analysis was performed to classify the slope roughness of the study area. A slope roughness of <18.15 was coded as 1, whereas that of >63.34 was coded as 7 (Table 5).

**Table 5.** Slope roughness codes.

Grade Range of Slope Roughness (°)	Code
Above 63.34	7
56.80–63.33	6
49.47–56.79	5
41.02–49.46	4
31.21–41.01	3
18.16–31.20	2
Below 18.15	1

- Aspect (*As*)

Each slope has a different aspect. Aspect refers to the inclination direction of a slope and affects wind flow and rainfall distribution. In this study, using DEM and ArcGIS aspect analysis, the aspect data of each grid were obtained. The inclination angle may be as follows: north, northeast, east, southeast, south, southwest, west, northwest, and flat ground (clockwise). In this study, a flat ground was coded as 1, whereas the southwestern part of a windward side was coded as 6 (Table 6).

**Table 6.** Aspect codes.

Aspect	Inclination Angle (°)	Code
Flat ground	—	1
Northeast	22.5–67.5°	2
East	67.5–112.5°	3
Southeast	112.5–157.5°	4
South	157.5–202.5°	5
Southwest	202.5–247.5°	6
West	247.5–292.5°	5
Northwest	292.5–337.5°	4
North	337.5–0° 0–22.5°	3

- Surface Roughness (*Tr*)

Surface roughness reflects the changes in a surface (standard deviation). Higher degrees of surface roughness indicate higher extents of changes, which may facilitate landslide occurrence. In the present study, cluster analysis was performed to classify the surface roughness of the study area. A surface roughness of <417.62 was coded as 1, whereas that of >2298.55 was coded as 7 (Table 7).

**Table 7.** Surface roughness codes.

Grade Range of Surface Roughness (m)	Code
Above 2298.55	7
2114.26–2298.54	6
1849.33–2114.25	5
1457.87–1849.32	4
957.51–1457.86	3
417.63–957.50	2
Below 417.62	1

- Distance from the River ( $D_r$ )

The distance of an area from a water body may affect the occurrence of landslides. A shorter distance is associated with higher levels of groundwater, which softens soil, thereby facilitating landslide occurrence. We used a river map to calculate the distance of each grid from a river; for this, the ArcGIS buffer analysis function was used. The analysis results were coded as shown in Table 8.

**Table 8.** Codes corresponding to the distance of an area from a water body.

Grade Range of Distance from the River (m)	Code
Below 350	7
351–700	6
701–1050	5
1051–1400	4
1401–1750	3
1751–2100	2
Above 2101	1

- Geology ( $G_s$ )

We used the geological map of the Central Geological Survey of the Ministry of Economic Affairs (2021) to obtain information on the geological conditions corresponding to each grid in the study area. On the basis of geological age and lithological data, it was divided into four strengths: very weak, medium, medium strong, and strong [40]. The highest strength was coded as 1, whereas the lowest strength was coded as 4 [38].

#### Slope Disturbance Factors

Using RTC with texture analysis for image interpretation and classification, we assessed the slope disturbance of the research area. The following six factors were included in further analysis: road density, building density, farmland planting rate, forest density, grassland density, and bare density. To quantify the slope disturbance in each basic grid, slope disturbance was defined as the area percentage ratio of each disturbance factor in each basic grid. The degree of land development of hillsides and its index were evaluated in reference to earlier studies [7,38]. Because we regarded environmental and slope disturbance factors as independent factors influencing landslides, a slope disturbance index was developed and is shown in Equation (7).

$$I_{DC} = \sum G_{DC} \times R \quad (7)$$

$DC$  refers to the disturbance condition.  $G_{DC}$  is a  $DC$  grade, which is the score corresponding to slope land use disturbance in each grid.  $R$  is the ratio of the area occupied by each slope and the utilization factor corresponding to the grid. Table 9 presents the grades corresponding to the  $DC$ s of the aforementioned six slope disturbance factors. For grading, we referred to a study conducted by Chen et al. [38].

**Table 9.** Scores of various slope disturbance factors.

Slope Disturbance Factor	Forest Density	Grassland Density	Farmland Planting Rate	Road Density	Building Density	Bare Density
Score	1	2	3	4	5	6

### Rainfall Trigger Factors

We obtained relevant data from the following 12 rainfall measurement stations within and near the study area: Weiliaoshan, Majia, Hongyeshan, Shangdewun, Dajin, Jinfeng, Ligang, Meinong, and Gusia [22] as well as Zhiben-5, Ali, and Sandimen [41]. Through inverse distance weighting (ArcGIS), the EAR and  $I_{3R,max}$  values were calculated for each station (Tables 10 and 11) for four rainfall events occurring in 2009 and 2013.

**Table 10.** EAR of each station after various rainfall events.

Management Unit	Station Code	Station Name	EAR (mm)			
			Morakot	0517 Rainfall	Soulik	Kongrey
CWB	C0R100	Weiliaoshan	1437.03	85.46	248.38	417.93
	C0R140	Majia	882.32	–	–	–
	C0S680	Hongyeshan	337.62	46.40	154.62	38.69
	C1R120	Shangdewun	1745.22	121.64	–	378.98
	C1V340	Dajin	–	168.74	129.19	–
	C1S820	Jinfeng	298.88	19.97	201.45	93.82
	C0R590	Ligang	466.82	–	–	233.36
	C0V310	Meinong	312.16	138.47	–	648.74
	C1R110	Gusia	492.67	269.31	87.05	263.33
WRA	01S210	Zhiben-5	91.57	16.49	130.31	54.73
	01Q910	Ali	1205	698.56	141.25	585.02
	01Q930	Sandimen	552.93	146.85	42.03	245.55

**Table 11.**  $I_{3R,max}$  of each station after various rainfall events.

Management Unit	Station Code	Station Name	$I_{3R,max}$ (mm/3 h)			
			Morakot	0517 Rainfall	Soulik	Kongrey
CWB	C0R100	Weiliaoshan	274	68.5	78	183.5
	C0R140	Majia	194	–	–	–
	C0S680	Hongyeshan	75	27.5	52.5	21
	C1R120	Shangdewun	206	83	–	153.5
	C1V340	Dajin	–	84	81	–
	C1S820	Jinfeng	199.5	12	108	25
	C0R590	Ligang	154.5	–	–	97
	C0V310	Meinong	114.5	61	–	176.5
	C1R110	Gusia	192	54	46.5	82
WRA	01S210	Zhiben-5	78	15	81	14
	01Q910	Ali	286	117	65	131
	01Q930	Sandimen	171	60	33	107

### 3.3.2. Analysis of Slope Environmental Strength Potential

We performed correlation analyses of environmental and slope disturbance factors. After highly correlated factors were eliminated, LR was performed to analyze the slope environmental strength; thus, a slope environmental strength regression model was constructed. Then, we established the index of slope environmental strength potential ( $I_{SESP}$ ). A basic

grid of 40 m × 40 m was constructed using ArcGIS; subsequently, the slope environmental strength potential value in each grid of the study area was calculated.

### Correlation Analyses of Slope Environmental Strength Potential Factors

The slope environmental strength potential factors initially selected in this study included environmental factors such as elevation, slope, aspect, slope roughness, surface roughness, distance from the river, and geology and slope disturbance factors. To ensure that the factors were independent and exerted no mutual effects, we performed correlation analyses of the selected factors before LR analysis to identify the degree of correlations between the factors. Elevation, slope, slope roughness, surface roughness, and slope disturbance index served as continuous variables, whereas aspect, distance from the river, and geology served as categorical variables. In LR, categorical variables only represent the data distribution of factor codes and not the effects of the code size on dependent variables. Hence, we focused only on continuous variables. Statistical analysis was performed using SPSS [42]. For the four rainfall events, the correlations between the factors were investigated through Pearson correlation analysis. If the absolute value of the correlation coefficient is closer to 0, the degree of correlation is weaker; in contrast, if it is closer to 1, the degree of correlation is stronger. Table 12 presents the correlations between the slope environmental strength potential factors. Elevation exhibited high-level correlations with surface roughness. Slope exhibited medium-to-high-level correlation with slope roughness. The remaining factors exhibited low-level correlations. Hence, surface roughness was not included in the LR model.

**Table 12.** Correlations between the slope environmental strength potential factors.

		Elevation ( <i>El</i> )	Slope ( <i>Sl</i> )	Slope Roughness ( <i>Slr</i> )	Surface Roughness ( <i>Tr</i> )	IDC
Elevation ( <i>El</i> )	Correlation	1				
	Significance (Two-tailed)					
	N	170,651				
Slope ( <i>Sl</i> )	Correlation	0.299 **	1			
	Significance (Two-tailed)	0.000				
	N	170,651	170,651			
Slope Roughness ( <i>Slr</i> )	Correlation	0.473 **	0.731 **	1		
	Significance (Two-tailed)	0.000	0.000			
	N	170,651	170,651	170,651		
Surface Roughness ( <i>Tr</i> )	Correlation	1.000 **	0.299 **	0.473 **	1	
	Significance (Two-tailed)	0.000	0.000	0.000		
	N	170,651	170,651	170,651	170,651	
IDC	Correlation	−0.369 **	−0.282 **	−0.363 **	−0.369 **	1
	Significance (Two-tailed)	0.000	0.000	0.000	0.000	
	N	170,651	170,651	170,651	170,651	170,651

Note: \*\* Correlation is significant at 0.01 level (two-tailed).

### Results of the Analysis of Slope Environmental Strength Potential

To reduce errors due to the evaluation model and subjective errors due to selection bias (human errors), we randomly sampled the same number of landslide and non-landslide

samples. After sampling, the data were randomly divided into training (70%) and test (30%) datasets. An environmental strength assessment model was constructed through LR [42].

The dependent variable was landslide or non-landslide, and the independent variables were environmental factors such as slope, aspect, elevation, distance from the river, slope roughness, geology, and slope disturbance factors. Through LR, a regression formula was developed for analyzing the slope environmental strength potential. The formula is shown in Equation (8).

$$L = \alpha + \beta_1 \times El + \beta_2 \times Sl + \beta_3 \times Slr + \beta_4 \times I_{DC} + \sum_{i=1}^4 \beta_{As,i} D_{As,i} + \sum_{i=1}^6 \beta_{Dr,i} D_{Dr,i} + \sum_{i=1}^3 \beta_{Gs,i} D_{Gs,i} \tag{8}$$

where *El* denotes the elevation, *Sl* is the slope, *Slr* is the slope roughness, *I<sub>DC</sub>* is the slope disturbance index, *As* is the aspect grade, *Dr* is the distance from the river, *Gs* is the geological grade,  $\beta$  is the regression coefficient of continuous variables, and  $\alpha$  is a constant. *D* represents a dummy variable, which is a value coded for the category corresponding to a factor. Substituting each regression coefficient and constant value into Equation (8) and substituting it into Equation (9), we can calculate the probability value of each grid, which represents the value of *I<sub>SESP</sub>*.

$$P = \frac{1}{1 + e^{-L}} \tag{9}$$

LR was performed to evaluate the training classification results of various rainfall events. The accuracies of classifications performed using the training and test data after 2009 Typhoon Morakot were 68.3% and 68.1%, respectively. Training data were used to deduce the accuracies of classifications for the entire study area. The estimated accuracy was 65.2% (Table 13). Table 14 presents the errors in the evaluation of various rainfall events. The accuracies of classifications performed using training data after the 0517 rainfall, Typhoon Soulik, and Typhoon Kongrey were 83.8%, 86.2%, and 86.4%, respectively; the corresponding values for the test datasets were 84.3%, 86.4%, and 87.5%. The average accuracy of the overall classification was approximately 80.4%.

**Table 13.** Errors in the evaluation of Typhoon Morakot.

		Training			Testing			Overall			
		Predicted		Accuracy (%)	Predicted		Accuracy (%)	Predicted		Accuracy (%)	
		Non-landslide	Landslide		Non-landslide	Landslide		Non-landslide	Landslide		
Actual	Non-landslide	4021	1692	70.4	1787	712	71.5	105,419	57,025	64.9	
	Landslide	1946	3831	66.3	858	1572	64.7	2391	5816	70.9	
Overall accuracy				68.3				68.1			65.2

**Table 14.** Accuracies of the classifications performed using training and test data after the four rainfall events.

Rainfall Event	Accuracy		
	Training (%)	Testing (%)	Overall (%)
Typhoon Morakot	68.3	68.1	65.2
0517 Rainfall	83.8	84.3	83.5
Typhoon Soulik	86.2	86.4	87.3
Typhoon Kongrey	86.4	87.5	85.7
Average accuracy	81.2	81.6	80.4

### 3.3.3. Establishment of a Landslide Hazard Index

Higher values of slope environmental strength potential are associated with larger amounts of rainfall and thus higher probabilities of landslides. By referring to the study of Jan and Lee [4], we adjusted this, and  $I_{RT}$  can be calculated as shown in Equation (10).

$$I_{RT} = EAR \times I_{3R,max} \quad (10)$$

We established a landslide hazard index ( $I_{RL}$ ) using  $I_{RT}$  and  $I_{SESP}$ . The formula is shown in Equation (11).

$$I_{RL} = I_{RT} \times I_{SESP} \quad (11)$$

Higher values of  $I_{RL}$  indicate a higher probability of landslides. At a constant  $I_{RL}$ ,  $I_{RT}$  is inversely proportional to  $I_{SESP}$ . Thus, if  $I_{SESP}$  is relatively stable, a large amount of rainfall would induce landslides. In contrast, if  $I_{SESP}$  is low, only a small amount of rainfall would induce landslides. We used the following comprehensive indicators of rainfall-induced landslides [4]:  $I_{RL1}$ ,  $I_{RL10}$ ,  $I_{RL25}$ ,  $I_{RL50}$ , and  $I_{RL90}$ . The index development method is described below.

1.  $I_{RL1}$ : From the  $I_{RL}$  values corresponding to the grid data of all rainfall-induced landslides in the study area, the value with a cumulative probability of 1% is selected (Weber's method) and is indicated as  $I_{RL1}$ . Grids with  $I_{RL}$  values less than that of  $I_{RL1}$  have landslide probabilities of <1%.
2.  $I_{RL10}$ : From the  $I_{RL}$  values corresponding to the grid data of all rainfall-induced landslides in the study area, the value with a cumulative probability of 10% is selected (Weber's method) and is indicated as  $I_{RL10}$ . Grids with  $I_{RL}$  values between the values of  $I_{RL1}$  and  $I_{RL10}$  have landslide probabilities of 1%–10%.
3.  $I_{RL90}$ : Landslide and non-landslide grids with values less than that of  $I_{RL10}$  are excluded. From the  $I_{RL}$  values corresponding to the remaining grids, the value with a cumulative probability of 90% (Weber's method) is selected and indicated as  $I_{RL90}$ . Grids with  $I_{RL}$  values exceeding that of  $I_{RL90}$  have landslide probabilities of >90%.
4.  $I_{RL10}$ – $I_{RL90}$ : To determine a landslide probability corresponding to a comprehensive index between  $I_{RL10}$  and  $I_{RL90}$ , the relationship between the aforementioned index and landslide probability can be expressed as shown in Equation (12).

$$\frac{I_{RLi} - I_{RL10}}{I_{RL90} - I_{RL10}} = \frac{P - 0.1}{0.9 - 0.1} \quad (12)$$

Equation (12) can be rewritten as Equation (13).

$$I_{RLi} = I_{RL10} + \Delta I_{RL} \left( \frac{P - 0.1}{0.8} \right) \quad (13)$$

where  $\Delta I_{RL} = I_{RL90} - I_{RL10}$ . Thus, the landslide probability corresponding to the landslide comprehensive index  $I_{RLi}$  can be obtained.

## 4. Discussion

### 4.1. Correlation between Slope Environmental Strength Potential and Rainfall-Induced Landslide

We first explored the distribution of landslide and non-landslide grids with the same  $I_{RL}$  value for each event and performed stratified random sampling according to the ratio of the numbers of landslide and non-landslide grids with the same  $I_{RL}$  value. To calculate the  $I_{RL}$  values corresponding to  $I_{RL1}$ ,  $I_{RL10}$ ,  $I_{RL25}$ ,  $I_{RL50}$ , and  $I_{RL90}$ , after merging the data points of each rainfall event, we sorted the landslide grids; then, using Equation (12), the  $I_{RL}$  values corresponding to different cumulative probabilities were calculated. Table 15 presents the  $I_{RL}$  indices and the corresponding values.

**Table 15.** Various  $I_{RL}$  values.

Various $I_{RL}$	$I_{RL}$ Value
$I_{RL1}$	1417.30
$I_{RL10}$	6563.47
$I_{RL25}$	28,307.89
$I_{RL50}$	64,548.59
$I_{RL90}$	122,533.70

Using the  $I_{RL}$  indices presented in Table 15, the correlation between  $I_{RT}$  and slope environmental strength potential was calculated after merging the data points of each rainfall event (Figure 6). The product of  $I_{RT}$  and  $I_{SESP}$  was the closest to the grids with different cumulative probabilities. The trend line corresponding to each  $I_{RL}$  value was drawn using the power method. As shown in Figure 5, the  $I_{RT}$  of 2009 Typhoon Morakot was the highest among the four rainfall events; thus, most of its landslide grids were distributed above  $I_{RL50}$ . For the 0517 rainfall in 2013, the grids were mostly below  $I_{RL90}$ . The  $I_{RT}$  of 2013 Typhoon Soulik was the lowest among the four rainfall events; most of its landslide grids were distributed below  $I_{RL25}$ , while the  $I_{RT}$  of 2013 Typhoon Kongrey was higher than those of the Typhoon Soulik and 0517 rainfall events; for Typhoon Kongrey, the grids were distributed between  $I_{RL1}$  and  $I_{RL90}$ .

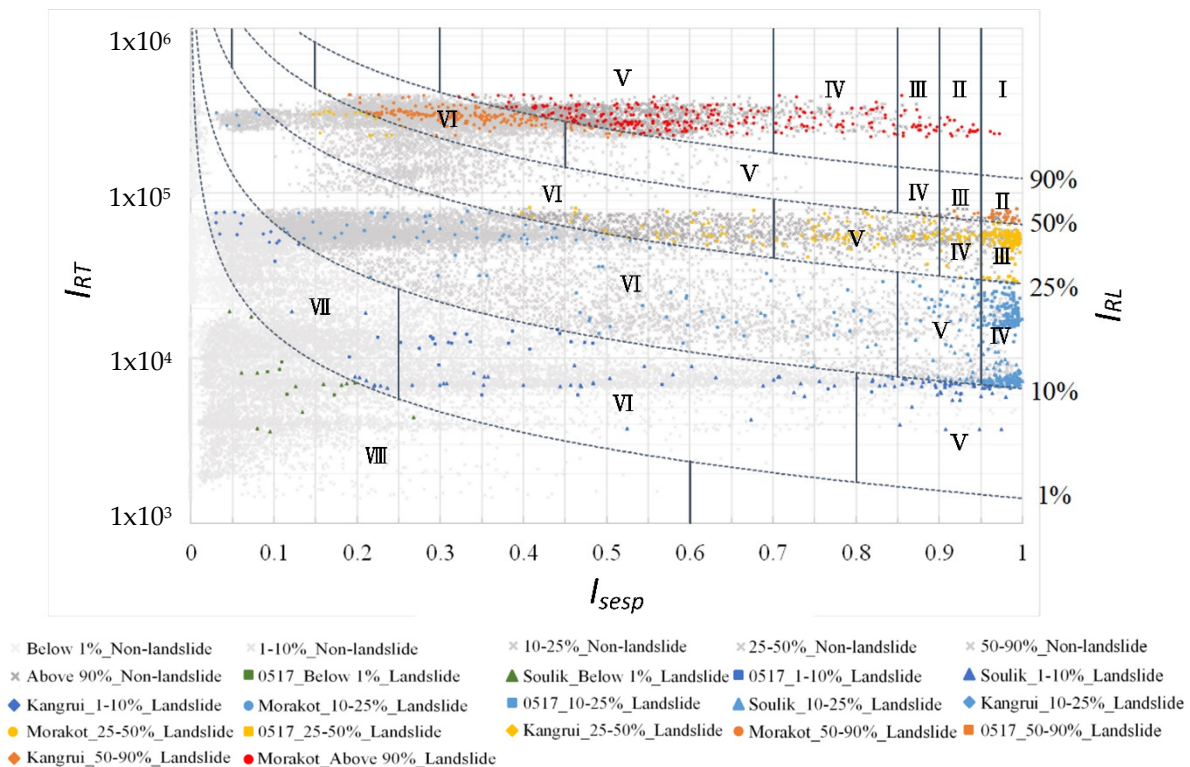


**Figure 6.** Slope environmental strength potential index versus rainfall trigger index.

#### 4.2. Evaluation of Landslide Hazards to Land Use

After the classification of  $I_{RL}$  indices with different cumulative probabilities, the number of landslide and non-landslide grids with different  $I_{SESP}$  grades and the landslide ratio (landslide/non-landslide) were estimated. Considering that higher values of  $I_{RT}$  are associated with higher values of  $I_{SESP}$  (and higher degrees of hazard), we investigated the most reasonable average distribution of the landslide ratio in an inductive manner. Then, the degree of hazard was calculated for each distribution situation and substituted into the

grids of each event. Thus, the hazard degree of rainfall-induced landslide in each grid of each event was obtained. Table 16 presents the landslide ratios (before and after induction) of various  $I_{SESP}$  grades of different  $I_{RL}$  indices. The same color in the table represents the same category of landslide ratio intervals ( $n = 8$ ). Figure 6 illustrates the results presented in Table 16. The landslide ratio intervals were normalized using the average landslide ratio of the same interval, as shown in Equation (14).

$$Z_{norm} = \left( \frac{X - X_{min}}{X_{max} - X_{min}} \right) \tag{14}$$

where  $Z_{norm}$  represents the value after normalization,  $X$  represents the value to be normalized,  $X_{min}$  represents the minimum value in the data, and  $X_{max}$  represents the maximum value in the data. In this study, the normalized value was regarded as the degree of rainfall-induced landslide hazard. The estimated degree of hazard was substituted into the grid of each rainfall event to obtain the degree of hazard corresponding to each rainfall event grid in the study area. The normalized value is a value between 0 and 1. Landslide probabilities of ( $I_{RL}$ ) of <1% still represent the possibility of landslide. Therefore, the minimum value of  $I_{RL1}$  indicates its risk probability. Table 17 presents the hazard value of each landslide ratio interval. The color reference in Table 17 is the same as that in Table 16. The hazard value of each grid of each rainfall event was substituted into each grid, and hazard maps were constructed. Higher degrees of hazard indicate higher probabilities of landslide and vice versa.

The hazard value of each interval was substituted into each grid of each rainfall event, and the hazard maps of the study area after each rainfall event were constructed (Figure 7). Hazard degree was classified into eight grades, and the classification was based on the method in Table 17. The  $I_{RT}$  of 2009 Typhoon Morakot was the highest among all rainfall events, and the number of landslide grids was 8207; thus, the degree of landslide hazard in the study area after this typhoon was the highest. The  $I_{RT}$  of 2013 Typhoon Kongrey was higher than that of 0517 rainfall in 2013; thus, the degree of landslide hazard after Typhoon Kongrey was higher than that after 0517 rainfall in 2013. The  $I_{RT}$  of 2013 Typhoon Soulik was the lowest, and the number of landslide grids was also the lowest ( $n = 3969$ ); thus, the degree of landslide hazard after this typhoon was the lowest.

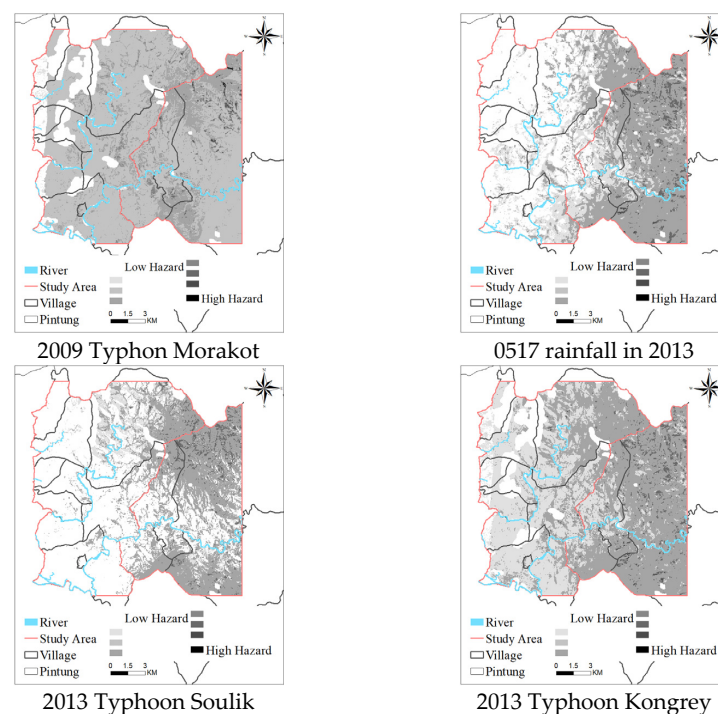


Figure 7. Potential maps of landslide hazards to land use after various rainfall events.

**Table 16.** Landslide ratios of various  $I_{SESP}$  grades of different  $I_{RL}$  classifications.

$I_{SESP}$	Below $I_{RL1}$			$I_{RL1}-I_{RL10}$			$I_{RL10}-I_{RL25}$			$I_{RL25}-I_{RL50}$			$I_{RL50}-I_{RL90}$			Above $I_{RL90}$			
	Landslide	Non-landslide	Landslide Ratio	Landslide	Non-landslide	Landslide Ratio	Landslide	Non-landslide	Landslide Ratio	Landslide	Non-landslide	Landslide Ratio	Landslide	Non-landslide	Landslide Ratio	Landslide	Non-landslide	Landslide Ratio	
0<0.05																			
0.05 < 0.10																			
0.10 < 0.15				26	6317	0.00412													
0.15 < 0.20																			
0.20 < 0.25																			
0.25 < 0.30																			
0.30 < 0.35	18	11,097	0.00162										196	4564	0.04294				
0.35 < 0.40										53	2889	0.01835							
0.40 < 0.45							101	8528	0.01184										
0.45 < 0.50																	184	1629	0.11295
0.50 < 0.55				56	3987	0.01405													
0.55 < 0.60																			
0.60 < 0.65																			
0.65 < 0.70													20	317	0.06309				
0.70 < 0.75																			
0.75 < 0.80																	51	148	0.34459
0.80 < 0.85										63	507	0.12426							
0.85 < 0.90																			
0.90 < 0.95				57	318	0.17925	55	368	0.14946				1	7	0.14286	22	19	1.15789	
0.95 < 1.00							255	294	0.86735	157	129	1.21705	27	131	0.20611	5	12	2.83333	
													29	17	1.70588	3	0	3	

**Table 17.** Hazard value of each interval.

Hazard Interval	Average Landslide Ratio	Hazard Value
Interval VIII	0.001	0.00001
Interval VII	0.004	0.00083
Interval VI	0.022	0.00673
Interval V	0.125	0.04142
Interval IV	0.39	0.1296
Interval III	0.93	0.30981
Interval II	2.27	0.7564
Interval I	3	1

## 5. Conclusions

In the present study, we developed an index to evaluate landslide hazards to land use after four prominent rainfall events in Sandimen and Wutai Townships in Pingtung County. Using RTC and texture analysis, we interpreted and classified the satellite images of the study area captured before and after four rainfall events. The average Kappa value was approximately 0.71, which indicated medium to high accuracy. A comparison of the satellite images captured before and after the rainfall events in terms of exposure revealed that the area of landslide due to 2009 Typhoon Morakot was the largest (1313.12 ha); the areas of landslides due to the other rainfall events were as follows: 0517 rainfall in 2013, 813.92 ha; Typhoon Kongrey, 789.44 ha; and Typhoon Soulik, 635.04 ha. Environmental factors (e.g., elevation, slope, aspect, slope roughness, distance from the river, and geology) and slope disturbance factors (e.g., road density, building density, farmland planting rate, forest density, grassland density, and bare density) were assessed in this study to analyze the slope environmental strength potential  $I_{SESP}$ . The average overall classification accuracy was approximately 80.4%.  $I_{RT}$  was calculated by multiplying EAR with  $I_{3R,max}$ . A new comprehensive index of rainfall-induced landslide  $I_{RL}$  ( $I_{RL} = I_{RT} \times I_{SESP}$ ) was established to determine the hazard of rainfall-induced landslides to land use. Using the correlation between  $I_{SESP}$  and  $I_{RT}$ , we determined the degrees of rainfall-induced landslide hazards to land use. At a constant  $I_{SESP}$ , higher values of  $I_{RT}$  indicate higher degrees of landslide hazard to land use; similarly, at a constant  $I_{RT}$ , higher values of  $I_{SESP}$  indicate higher degrees of landslide hazard to land use. Landslide occurrence is positively correlated with  $I_{RT}$  and  $I_{SESP}$ . In cases of large  $I_{SESP}$  values (e.g., fragile environment and high land development intensity), small  $I_{RT}$  values may cause landslides.

**Author Contributions:** Conceptualization, C.-M.T., Y.-R.C., C.-Y.T., and S.-C.H.; Methodology, C.-M.T. and Y.-R.C.; Investigation, C.-Y.T. and S.-C.H.; Writing—original draft preparation, C.-M.T. and Y.-R.C.; Writing—review, C.-M.T., Y.-R.C., C.-Y.T., and S.-C.H.; Editing, C.-M.T. and Y.-R.C.; Supervision, C.-M.T. All authors have read and agreed to the published version of the manuscript.

**Funding:** This research received no external funding.

**Data Availability Statement:** Data is contained within the article.

**Acknowledgments:** This work was supported in part by grants from the Taiwan National Science and Technology Council (NSTC 111-2625-M-309-001 and NSTC 112-2625-M-006-023).

**Conflicts of Interest:** The authors declare no conflicts of interest.

## References

1. *Disaster Management White Paper*; Central Disaster Prevention and Response Council, Executive Yuan: Taipei, Taiwan, 2012.
2. Lin, C.W.; Chang, W.S.; Liu, S.H.; Tsai, T.T.; Lee, S.P.; Tsang, Y.C.; Shieh, C.L.; Tseng, C.M. Landslides triggered by the 7 August 2009 Typhoon Morakot in Southern Taiwan. *Eng. Geol.* **2011**, *123*, 3–12. [[CrossRef](#)]

3. National Disasters Prevention and Protection Commission. *Typhoon Morakot Disaster Responses Reports from Typhoon Morakot Central Emergency Operating Center 74th Report*, National Disasters Prevention and Protection Commission: New Taipei City, Taiwan, 2009.
4. Jan, C.D.; Lee, M.H. A debris-flow rainfall-based warning model. *J. Chin. Soil Water Conserv.* **2004**, *35*, 275–285.
5. Chen, Y.R.; Tsai, K.J.; Hsieh, S.C.; Ho, Y.L. Evaluation of Landslide Potential due to Land Use in the Slope. *Electron. J. Geotech. Eng.* **2015**, *20*, 4277–4292.
6. Jan, C.D.; Yang, S.Y.; Su, Y.W.; Haung, W.S. Investigation about rainfall-induced shallow landslides in CYL and TWR watersheds, Taiwan. *Environ. Earth Sci.* **2016**, *75*, 898. [[CrossRef](#)]
7. Tseng, C.M.; Chen, Y.R.; Wu, S.M. Scale and spatial distribution assessment of rainfall-induced landslides in a catchment with mountain roads. *Nat. Hazards Earth Syst. Sci.* **2018**, *18*, 687–708. [[CrossRef](#)]
8. Chen, C.W.; Tung, Y.S.; Liou, J.J.; Li, H.C.; Cheng, C.T.; Chen, Y.M.; Oguchi, T. Assessing landslide characteristics in a changing climate in northern Taiwan. *Catena* **2019**, *175*, 263–277. [[CrossRef](#)]
9. Lee, C.F.; Chou, H.T.; Wei, L.W.; Huang, W.K.; Chi, S.Y.; Chen, S.C.; Huang, W.C. Geomorphic Evolution of The Dong-Ao Peak Landslide, North Eastern Taiwan. *J. Chin. Soil Water Conserv.* **2014**, *45*, 174–183.
10. Caracciolo, D.; Arnone, E.; Conti, F.L.; Noto, L.V. Exploiting historical rainfall and landslide data in a spatial database for the derivation of critical rainfall thresholds. *Environ. Earth Sci.* **2017**, *76*, 222. [[CrossRef](#)]
11. Chen, S.C.; Wu, C.Y. Establishment of Landslide Susceptibility Early Warning Model in National Forest Areas Based on Geo-intrinsic and Hydro-extrinsic Factors. *J. Chin. Soil Water Conserv.* **2018**, *49*, 89–97.
12. Shahabi, H.; Khezri, S.; Ahmad, B.B.; Hashim, M. Landslide susceptibility mapping at central Zab basin, Iran: A comparison between analytical hierarchy process frequency ratio and logistic regression models. *Catena* **2014**, *115*, 55–70. [[CrossRef](#)]
13. Dai, F.C.; Lee, C.F.; Ngai, Y.Y. Landslide risk assessment and management: An overview. *Eng. Geol.* **2002**, *64*, 65–87. [[CrossRef](#)]
14. Ayalew, L.; Yamagishi, H. The application of GIS-based logistic regression for landslide susceptibility mapping in the Kakuda-Yahiko Mountains, Central Japan. *Geomorphology* **2005**, *65*, 15–31. [[CrossRef](#)]
15. Chau, K.T.; Chan, J.E. Regional bias of landslide data in generating susceptibility maps using logistic regression: Case of Hong Kong Island. *Landslides* **2005**, *2*, 280–290. [[CrossRef](#)]
16. Chen, Z.; Wang, J. Landslide hazard mapping using logistic regression model in Mackenzie Valley, Canada. *Nat. Hazards* **2007**, *42*, 75–89. [[CrossRef](#)]
17. Lee, S.; Pradhan, B. Landslide hazard mapping at Selangor, Malaysia using frequency ratio and logistic regression models. *Landslides* **2007**, *4*, 33–41. [[CrossRef](#)]
18. Sun, X.; Chen, J.; Bao, Y.; Han, X.; Zhan, J.; Peng, W. Landslide Susceptibility Mapping Using Logistic Regression Analysis along the Jinsha River and Its Tributaries Close to Derong and Deqin County, Southwestern China. *ISPRS Int. J. Geo-Inf.* **2018**, *7*, 438. [[CrossRef](#)]
19. Wubalem, A.; Meten, M. Landslide susceptibility mapping using information value and logistic regression models in Goncha Siso Eneses area, northwestern Ethiopia. *SN Appl. Sci.* **2020**, *2*, 807. [[CrossRef](#)]
20. Sujatha, E.R.; Sridhar, V. Landslide Susceptibility Analysis: A Logistic Regression Model Case Study in Coonor, India. *Hydrology* **2021**, *8*, 41. [[CrossRef](#)]
21. Pingtung County Government, Taiwan. 2022. Available online: <https://www.pthg.gov.tw/en/Default.aspx> (accessed on 1 October 2022).
22. Central Weather Bureau. 2021. Available online: <https://www.cwb.gov.tw/eng/> (accessed on 1 January 2021).
23. Central Geological Survey, Ministry of Economic Affairs. 2022. Available online: <https://www.moeacgs.gov.tw/> (accessed on 1 January 2022).
24. Neipu Household Registration Office, Pingtung County Government, Taiwan. 2022. Available online: <https://www.neipu.gov.tw/Default.aspx> (accessed on 11 November 2022).
25. Sandimen Township Office, Pingtung County Government, Taiwan. 2022. Available online: <https://www.pthg.gov.tw/sandimen/Default.aspx> (accessed on 11 November 2022).
26. Wutai Township Office, Pingtung County Government, Taiwan. 2022. Available online: <https://www.wutai.gov.tw/index.php> (accessed on 11 November 2022).
27. Maolin National Scenic Area Administration, Tourism Bureau, MOTC. 2022. Available online: <https://www.maolin-nsa.gov.tw/EN/> (accessed on 11 November 2022).
28. Lin, C.W.; Shieh, C.J.; Yuan, B.D.; Shieh, Y.C.; Huang, M.L.; Lee, S.Y. Impact of Chi-Chi earthquake on the occurrence of landslides and debris flows: Example from the Chenyulan River watershed, Nantou, Taiwan. *Eng. Geol.* **2004**, *71*, 49–61. [[CrossRef](#)]
29. ERDAS. *ERDAS IMAGINE®Tour Guide*; ERDAS World Headquarter: Atlanta, GA, USA, 2011.
30. Seo, K.; Funasaki, M. Relationship between sediment disaster (mainly debris flow damage) and rainfall. *Int. J. Erosion Control Eng.* **1973**, *26*, 22–28.
31. Chen, C.Y.; Chen, T.C.; Yu, F.C.; Yu, W.H.; Tseng, C.C. Rainfall duration and debris-flow initiated studies for real-time monitoring. *Environ. Geol.* **2005**, *47*, 715–724. [[CrossRef](#)]
32. ESRI. ArcGIS. 2019. Available online: <https://www.esri.com/en-us/home> (accessed on 1 September 2019).
33. Hosmer, D.W.; Lemeshow, S. *Applied Logistic Regression*, 2nd ed.; Wiley: Hoboken, NJ, USA, 2000; ISBN 978-0-471-35632-5.
34. Cox, D.R. *The Analysis of Binary Data*; Methuen: London, UK, 1970.

35. Ohlmacher, G.C.; Davis, J.C. Using multiple logistic regression and GIS technology to predict landslide hazard in northeast Kansas, USA. *Eng. Geol.* **2003**, *69*, 331–343. [[CrossRef](#)]
36. Verbyla, D.L. *Satellite Remote Sensing of Natural Resources*; CRC Press: New York, NY, USA, 1995.
37. Cohen, J. A coefficient of agreement for nominal scales. *Educ. Psychol. Meas.* **1960**, *20*, 37–46. [[CrossRef](#)]
38. Chen, Y.R.; Chen, J.W.; Hsieh, S.C.; Ni, P.N. The Application of Remote Sensing Technology to the Interpretation of Land Use for Rainfall-Induced Landslides Based on Genetic Algorithms and Artificial Neural Networks. *IEEE J. Sel. Top. Appl. Earth Obs. Remote Sens.* **2009**, *2*, 87–95. [[CrossRef](#)]
39. Regulations of soil and water conservation, Soil and Water Conservation Bureau. 2022. Available online: [https://www.ardswc.gov.tw/Home/eng/Info/item\\_list?mid=392](https://www.ardswc.gov.tw/Home/eng/Info/item_list?mid=392) (accessed on 26 March 2024).
40. ISRM. *Rock Characterization, Testing and Monitoring*; Pergamon Press: Oxford, UK, 1981.
41. Water Resources Agency, Ministry of Economic Affairs. 2021. Available online: <https://www.wra.gov.tw/> (accessed on 1 January 2021).
42. SPSS. *SPSS 14.0 Brief Guide*; SPSS Inc.: Chicago, IL, USA, 2005.

**Disclaimer/Publisher’s Note:** The statements, opinions and data contained in all publications are solely those of the individual author(s) and contributor(s) and not of MDPI and/or the editor(s). MDPI and/or the editor(s) disclaim responsibility for any injury to people or property resulting from any ideas, methods, instructions or products referred to in the content.